

Dual-Wave Acoustofluidic Centrifuge for Ultrafast Concentration of Nanoparticles and Extracellular Vesicles

Povilas Dumčius, Roman Mikhaylov, Xiaoyan Zhang, Matthew Bareford, Mercedes Stringer, Rachel Errington, Chao Sun, Esperanza Gonzalez, Tomaš Krukovski, Juan M Falcon-Perez, Dongfang Liang, Yong-Qing Fu, Aled Clayton, and Xin Yang*

Extracellular vesicles (EVs) are secreted nanostructures that play various roles in critical cancer processes. They operate as an intercellular communication system, transferring complex sets of biomolecules from cell to cell. The concentration of EVs is difficult to decipher, and there is an unmet technological need for improved (faster, simpler, and gentler) approaches to isolate EVs from complex matrices. Herein, an acoustofluidic concentration of extracellular vesicles (ACEV) is presented, based on a thin-film printed circuit board with interdigital electrodes mounted on a piezoelectric substrate. An angle of 120° is identified between the electrodes and the reference flat of the piezoelectric substrate for simultaneous generation of Rayleigh and shear horizontal waves. The dual waves create a complex acoustic field in a droplet, resulting in effective concentration of nanoparticles and EVs. The ACEV is able to concentrate 20 nm nanospheres within 105 s and four EV dilutions derived from the human prostate cancer (Du145) cell line in approximately 30 s. Cryo-electron microscopy confirmed the preservation of EV integrity. The ACEV device holds great potential to revolutionize investigations of EVs. Its faster, simpler, and gentler approach to EV isolation and concentration can save time and effort in phenotypic and functional studies of EVs.


1. Introduction

Extracellular vesicles (EVs), including ectosomes, exosomes, and other cell-derived vesicular materials, are essential modalities for intercellular communication.^[1] EVs play critical roles in transmitting signal-initiating elements and nucleic acids within the immediate pericellular space and over long distances.^[2] Such events contribute to homeostatic control of tissue environments^[3] and orchestrate adaptive changes such as angiogenesis^[4] and inflammation.^[5] Body fluids, including blood, urine, saliva, and cerebral spinal fluid (CSF), contain EVs with important information about pathogenic processes, including metabolic and infectious diseases. They may critically aid clinical diagnosis, disease monitoring and prognosis in various diseases including cancer. Therefore, many assay systems are being developed to quantify and detect EV-associated biomarkers.^[6]

P. Dumčius, R. Mikhaylov, X. Zhang, M. Stringer, X. Yang
Department of Electrical and Electronic Engineering
School of Engineering
Cardiff University
Cardiff CF243AA, UK
E-mail: yangx26@cardiff.ac.uk

M. Bareford, R. Errington, A. Clayton
Tissue Micro-Environment Group
Division of Cancer & Genetics
School of Medicine
Cardiff University
Cardiff CF144XN, UK

C. Sun
School of Life Sciences
Northwestern Polytechnical University
Xi'an, P. R. China

 The ORCID identification number(s) for the author(s) of this article can be found under <https://doi.org/10.1002/smll.202300390>.

© 2023 The Authors. Small published by Wiley-VCH GmbH. This is an open access article under the terms of the Creative Commons Attribution-NonCommercial-NoDerivs License, which permits use and distribution in any medium, provided the original work is properly cited, the use is non-commercial and no modifications or adaptations are made.

DOI: 10.1002/smll.202300390

E. Gonzalez, J. M. Falcon-Perez
Exosomes Laboratory
CIC bioGUNE-BRTA
CIBERehd
Bizkaia Technology Park
Bilbao 48160, Spain

T. Krukovski
Department of Electrical Engineering and Sensor Technology
Institute of Engineering
Hanze University Groningen
AS Groningen 119747, Netherlands

J. M. Falcon-Perez
Centro de Investigación Biomédica en Red de Enfermedades Hepáticas Y Digestivas (CIBERehd)
Madrid 28029, Spain

J. M. Falcon-Perez
IKERBASQUE
Basque Foundation for Science
Bilbao 48011, Spain

D. Liang
Department of Engineering
University of Cambridge
Cambridge CB2 1PZ, UK

Y.-Q. Fu
Faculty of Engineering and Environment
Northumbria University
Newcastle upon Tyne NE1 8ST, UK

Successful clinical applications of EVs depend on vesicle separation and selective concentration from the non-vesicular constituents of the biospecimen. One of the most widely used methods for this purpose is ultracentrifugation,^[7,8,9] where a large centrifugal force is applied to sediment nano-vesicles, sometimes through dense media such as iodixanol. As objects of different masses and densities are affected differently by the gravitational fields, particles in the nanometre size range will be slower to sediment and, in turn, require longer processing times (up to eight hours).^[10,11] In addition, this is a laborious process, requiring expensive infrastructure and safety considerations. Other methods, such as size exclusion chromatography,^[12] have attracted extensive attention as a more tractable approach for biomolecule separation, retaining structurally intact vesicles albeit at rather low concentrations. Alternative methods include flow field-flow fractionation,^[13] optical,^[14] dielectrophoretic,^[15] magnetic,^[16] hydrodynamic,^[17] and acoustic-based approaches.

Manipulation of bioparticles through acoustophoresis^[18] has gained significant attention due to its biocompatibility, ease of use, high efficiency, and low cost.^[19–21] Bioparticles can be sensed and manipulated by several acoustic wave modes, including thickness-shear mode, Love mode, and Rayleigh mode.^[22,23] Rayleigh waves are a type of surface acoustic wave (SAW) generated in a solid substrate (out-of-plane). Frequently, these waves are excited on a piezoelectric substrate, and when they are in contact with a fluid, energy is coupled into the fluid in the form of leaky acoustic waves. However, significant damping of the SAW amplitudes leads to loss of energy and effective manipulation of bioparticles. In contrast, minimum damping or attenuation of shear-horizontal SAW (SH-SAW) into the fluid is noted, as the SH-SAW travels in-plane on the substrate and their displacement are parallel to its surface.^[24] Most previous studies demonstrated concentrating bioparticles using Rayleigh SAW. Asymmetric SAW generated azimuthal bulk liquid recirculation, which gave rise to an inward radial force that concentrated particles and yeast cells (5–10 μm).^[25] Subsequently, by carefully manipulating SAW frequency, streaming and radiation forces were balanced for particle separation of 6 and 31 μm in a 2- μL sessile droplet,^[26] as well as 1 and 5 μm , 1 and 10 μm , 3 and 5 μm in the sample.^[27,28] The effective concentration of nanoparticles was also demonstrated by using chirped interdigital transducers (IDTs) producing SAWs in a glass capillary, in which nanomaterials ranging from 80 to 500 nm were enriched.^[29] An acoustofluidic multi-well plate utilized circular stranding flexural waves to enrich micro/nanoparticles and cells.^[30] Double-slanted IDTs were designed to yield a combination of acoustic streaming and droplet wobbling to break through the limitation of manipulating nanoparticles less than 100 nm. Rapid nanoparticle concentration and extracellular vesicle isolation/encapsulation were demonstrated, with the smallest size of 28 nm concentrated within 1 min in the samples up to 20 μL .^[31,32] To build upon this significant work the processing time, nano-size limit and especially the sample volume must further improve. Unequivocally, an affordable, accessible, and easy-to-manufacture package for nanoparticle manipulation is desirable.

This study presents an ultrafast acoustofluidic centrifuge for EVs (ACEV). To transcend the current limits, we have

developed a dual-wave mode which simultaneously generates both Rayleigh and SH-SAWs to induce acoustic streaming and oscillatory droplet deformation. These conditions effectively concentrate nanoparticles down to 20 nm within 105 s with a sample volume of 50 μL . The ACEV device demonstrates ultrafast concentration of EVs, where an EV aggregation is visible within seconds and by 30 s had produced EV pellets.

2. Experimental Section

2.1. Fabrication of the Acoustofluidic Centrifuge for EV (ACEV)

The IDT in the ACEV was developed using a TPCB technique as described.^[33] A TPCB patterned with interdigital electrodes was made by circuitfly.com, which consisted of dual metal bilayers (Au/Ni, 30 nm/2 μm) patterned on a 70 μm thick polyester laminate. The period of the interdigital electrode, electrode number, and aperture size were 200 μm , 40 pairs, and 13 mm, respectively. The TPCB was linked with a coaxial wire soldered to its bus pads and terminated with an SMA connector. A mechanical clamping method, as reported,^[34,35] was used for assembling the detachable interdigital electrodes on the TPCB onto a LiNbO₃ substrate (Figure S1, Supporting Information). The TPCB was attached to a TPCB clamp which forced it down; any changes in the angle between the TPCB and the LiNbO₃ substrate were done by releasing the TPCB clamp and then rotating the LiNbO₃ substrate. A template was designed to accurately position the angle between the TPCB and the reference flat of the LiNbO₃ substrate. The template was printed with ink on a round paper sheet and mounted underneath the substrate. The above mechanism allows a quick assembly of the IDT with arbitrary LiNbO₃ substrate angles as an example of 120° shown in **Figures 1a** and **2a**. To maintain consistency when adding samples, a polydimethylsiloxane (PDMS) ring (ID = 9 mm, OD = 10 mm) was mounted on the LiNbO₃ substrate and built by pouring PDMS into a 3D-printed mold.

2.2. Device Operation

Radio frequency (RF) signals were generated using a signal generator (RS Pro RSDG 5162) and amplified with an RF power amplifier (Mini-Circuits, USA). A matching network was designed for the ACEV device to match the impedance between the TPCB IDT and the amplifier's output stage.

2.3. Optimization of the ACEV Device with Various Angles

The frequency characteristics of the ACEV device were evaluated using the S-parameters. The reflection coefficient S_{11} of the ACEV device was recorded using a vector network analyzer (VNA, E5061B ENA, Keysight) during the rotation at an interval of 10°. At each angle, a working frequency was identified from the frequency corresponding to the minimum reflection on the S_{11} spectrum. We tested these frequencies' ability to generate wave modes to concentrate nanoparticles. Our investigation included the deformation measurements at the centre and

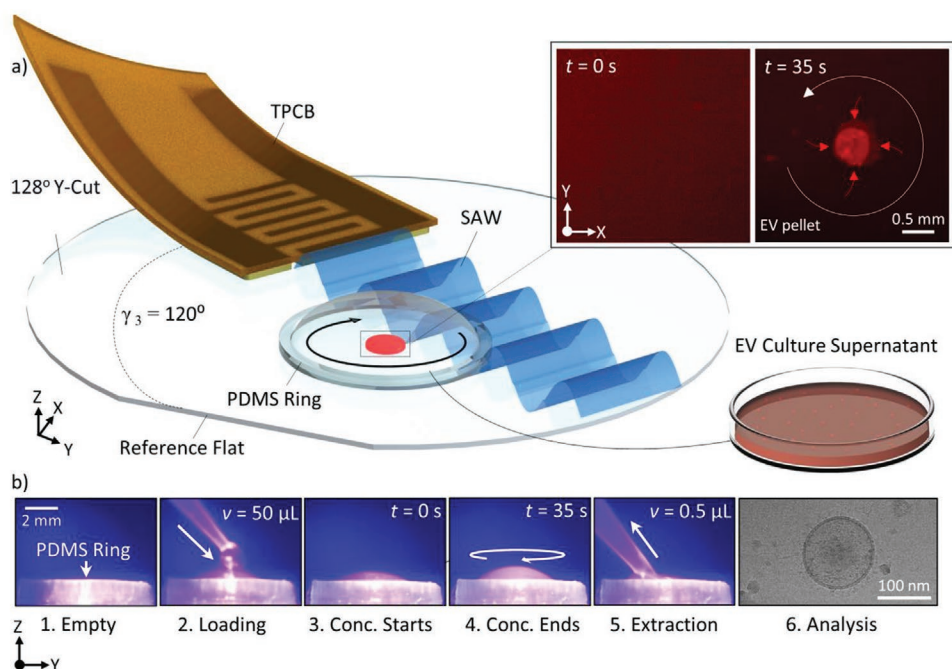


Figure 1. Acoustofluidic centrifuge for ultra-fast concentration of extracellular vesicles (ACEV). a) The ACEV device is made by mounting a thin-film printed circuit board (TPCB) with interdigital electrodes to a 128° Y-cut LiNbO₃ substrate. EV suspension is added to a PDMS ring as the sample reservoir. The concentration is achieved by the micro-streaming induced by surface acoustic wave (SAW), produced by the TPCB-based transducer. An inset shows the EV sample inside the PDMS ring before and after SAW concentration. b) Process flow for using the ACEV device. 1. The PDMS ring is prepared for accommodating EV culture supernatant. 2. An EV suspension (50-µL) is loaded into the PDMS ring. 3. SAW is turned on to concentrate the EV supernatant. 4. Extensive microstreaming is noted in the EV sample, rising the sample higher. 5. The concentrated EVs form a pellet, which can be extracted using a pipette. 6. Harvested EVs are subjected to follow-up analysis, such as electron microscopy.

periphery of the droplet surface, which revealed the oscillation of the sample. As shown in Figure 2b, a camera was placed next to the droplet to record the deformation on the centre and periphery (green, red, and blue arrows). The data was then analyzed using Tracker (physlets.org) to register the deformation on the z-axis.

2.4. Numerical Studies

A finite element model was built in COMSOL Software (Multiphysics 5.4, COMSOL Inc) to study the vibration pattern on the device surface and the interaction with the droplet. Piezoelectricity Multiphysics interface was used in the study. A trigonal crystal system with six elastic stiffness values, four piezoelectric tensors, and two dielectric coefficients was used to establish the piezoelectric characteristics. We utilized the piezoelectric coefficient values reported in Refs. [36] and [37]. Firstly, the crystal and IDT coordinate systems were defined as (α, β, γ) and (x, y, z) , respectively. Initially, the LiNbO₃ crystal and geometry coordinates were set to $(0, 0, 0)$. Since the 128° Y-cut LiNbO₃ substrate was used in the experiment, a Euler angle coordinate transformation of $(\alpha + 0^\circ, \beta + 38^\circ, \gamma + 0^\circ)$ was performed to describe the crystal cut angle. The rotation of the TPCB was simulated by rotating the substrate along γ for different angles. To compute the acoustic pressure distribution inside the droplet, the “Thermoviscous Acoustics” module in the COMSOL software was utilized.

2.5. Sample Preparation

The ACEV device’s ability to concentrate nanoparticles was validated using fluorescent polystyrene nanoparticles (Sigma Aldrich, USA) with their nominated sizes of 20, 30, 100, and 500 nm. These nanoparticles were prepared by diluting them into phosphate-buffered saline (PBS) at a $\approx 0.01 \text{ g mL}^{-1}$ concentration.

EVs were purified from Du145 prostate cancer cells, grown in bioreactors, by ultracentrifugation on a sucrose cushion as described.^[38] Briefly, the bioreactors were seeded with an initial optimized concentration of 4 million cells and cultured in RPMI media with PS/LG and 10% FBS. Upon seeding, 15 mL RPMI with PS/LG and EV depleted FBS were added to the cell compartment, and the standard RPMI + PS/LG + 10% FBS was used in the upper compartment. The bioreactors were left to culture for two weeks. The media from the cell compartment was then removed, processed to remove any cell/debris which was not EV and then frozen at -80°C until the ultracentrifugation step. The cell compartment was flushed and washed with RPMI media (no additives) before being replenished with 15 mL RPMI with PS/LG and EV-depleted FBS. The standard RPMI + PS/LG + 10% FBS used in the upper compartment was replaced afterwards. After the initial two weeks incubation period, this process was then repeated every week. Once enough samples were collected, EVs were purified using ultracentrifugation on a 30% sucrose/D2O.^[39] Purified EVs were resuspended in PBS, aliquoted and stored at -80°C .

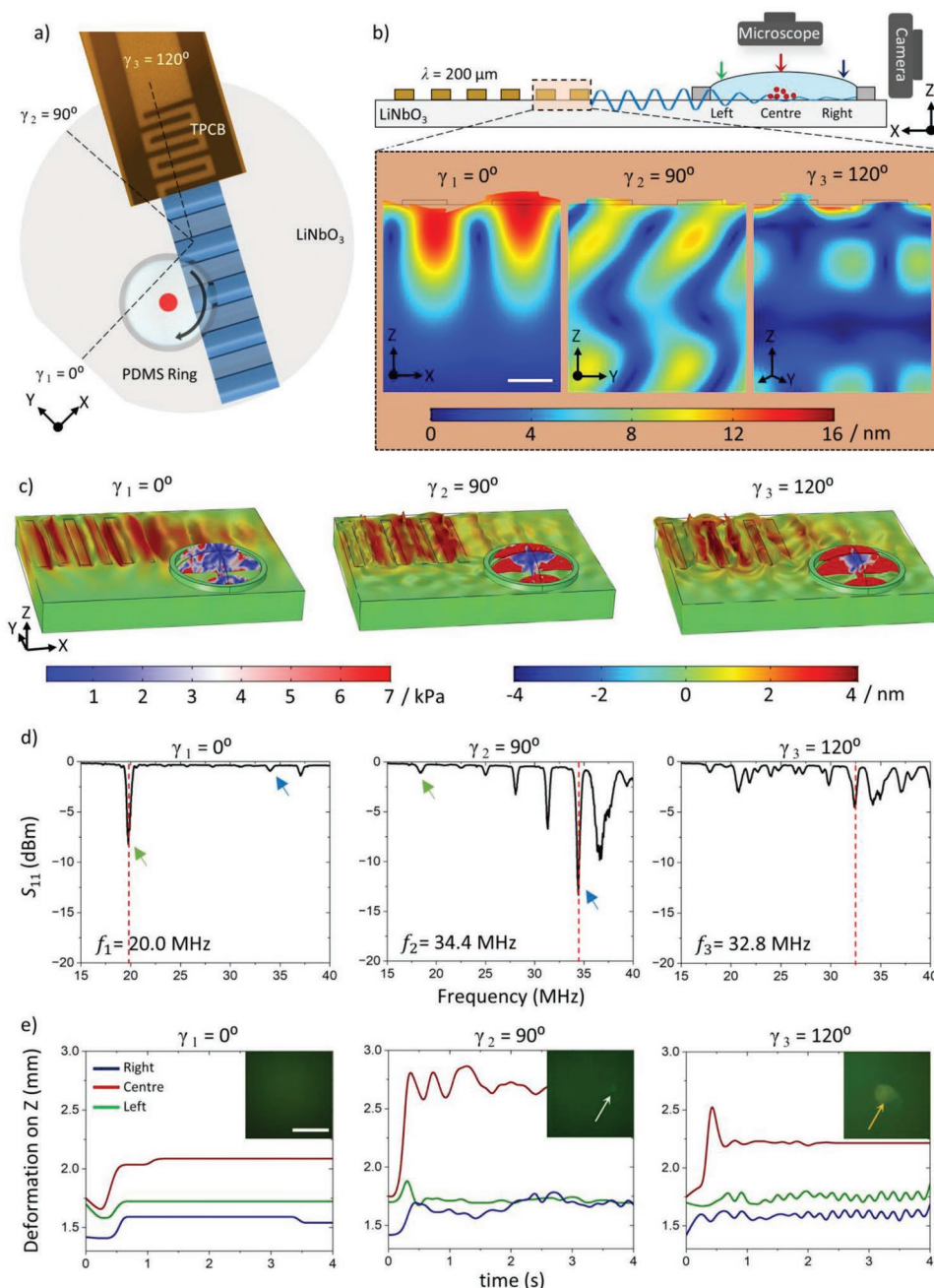


Figure 2. Characterization and optimization of the ACEV device. a) The top view drawing shows the FPCB rotating on the 128° Y-cut LiNbO₃ substrate. Three angles, $\gamma_1 = 0^\circ$, $\gamma_2 = 90^\circ$, and $\gamma_3 = 120^\circ$, with respect to the reference flat on the substrate, are selected for characterization. b) Schematic diagram of the SAW interacted with the droplet in the PDMS ring. Three arrows indicate the regions for measuring the droplet deformation on the z-axis. An inset shows the numerical simulations of the interdigital transducer (IDT) vibration under the three different TPCB angles. The scale bar is $50 \mu\text{m}$. c) 3D numerical simulations show different waveforms emerging from the IDT, resulting in various acoustic pressure patterns within the PDMS ring-constrained sample. d) The S_{11} parameter for the three TPCB angles indicates that the working frequency for the three angles is 20.0 MHz , 34.2 MHz , and 32.8 MHz , respectively. Blue and green arrows indicate SH-SAW and Rayleigh SAW, respectively. e) The droplet deformation on the z-axis is measured by three regions, as marked in Figure 2b. Insets demonstrate the manipulation of 20 nm particles at different angles. Scale bars 0.5 mm .

Once defrosted, the EVs were used in experiments and not re-frozen to avoid frost damage. These aliquots were then measured using nanoparticle tracking analysis (NTA) and a micro-BCA protein assay to ascertain EV-particle concentration and protein concentrations respectively. Quantification of

EV-particles and EV-protein was then repeated on the sample post-fluorescent labeling. To render these vesicles fluorescent for optical tracking, they were conjugated to Alexa-488 through a maleimide linker as described in.^[40] The original EV sample ($\approx 50 \mu\text{L}$) was then diluted and dispersed in $150 \mu\text{L}$

PBS. The sample concentration was further reduced to 1/40, then 1/400, and finally to 1/4000 to form a dilution range for testing. Control samples for cryo-electron microscope imaging and an immuno-assay to detect CD81 were prepared by adding 2 μL of EVs to 38 μL of PBS. Post-ACEV concentration pellets were collected using a pipette by manually extracting a fraction of the liquid (0.5 μL) near the concentration region, as depicted in Figure 4a. A sample of the equivalent volume was also taken from the peripheral, non-concentrated region. All these samples were stored immediately at -80°C .

Six mixtures (1 mL) of water and glycerol were prepared to simulate wide-ranging body fluids commonly rich with EVs for varied viscosity experiments (Figure 4e). The viscosity ratios were determined analytically and then confirmed using a capillary viscometer. The ratios (water/glycerol) were 1 and 0, 0.787 and 0.212, 0.695 and 0.300, 0.637 and 0.362, 0.590 and 0.410, 0.557 and 0.442 mL for viscosities 1, 2, 3, 4, 5 and 6 cP respectively. Furthermore, 100 nm fluorescent polystyrene particles (Sigma Aldrich, USA) were mixed into the solution at a dilution of 670×10^6 particles/mL. Both the preparation and experiments were performed at a room temperature of 20°C .

2.6. Nano-Particle Tracking Analysis (NTA)

The size and concentration of particles present within Du145 cell line-derived samples were measured using a NanoSight™ NS300 system (Malvern Instruments, Malvern, UK) as described.^[41] The instrument was calibrated with 80 nm silica beads, prior to each use (nanoComposix, San Diego, USA). Samples were diluted in particle-free water (Fresenius Kabi, Runcorn, UK), to concentrations up to 2×10^9 particles per mL. Data was collected at 25°C with a 488 nm laser and three videos of 60 s were taken in light scatter mode with the controlled fluid flow with a pump speed set to 50. Videos were processed using NTA 3.1 software (version 3.1 build 3.1.54), where minimum particle size, track length and blur were set at “automatic.” Background measurements of culture media, or water that had not been exposed to cells contained negligible particles.

2.7. Cryo-Electron Microscopy

EV samples were deposited onto glow-discharging holey carbon 200-mesh copper grids (Quantifoil, Micro Tools GmbH, Germany) and subjected to vitrification using a Vitrobot (Maas-tricht Instruments BV, The Netherlands). Imaging of vitrified samples was conducted at the liquid nitrogen temperature using a transmission cryo-electron microscope (JEM-2200FS/CR, JEOL, USA) with a field emission gun operated at an acceleration voltage of 200 kV. More than 600 individual EVs were analyzed using ImageJ (National Institutes of Health).

2.8. Plate-Based Immune-Labeling Assay

Purified EVs were immobilized on high-protein-binding ELISA plates (at doses of ≤ 10 μg per well) overnight in PBS. After

immobilization, 1% (w/v) BSA/PBS blocking solution was added, and the wells were blocked for two hours. CD81 Primary antibodies (at 2 $\mu\text{g}/\text{mL}$) were added and incubated for two hours. After three washes, the detection was by incubating the solution with goat anti-mouse biotinylated secondary antibodies (PerkinElmer Life) for 1 hour. Following three washes, Europium conjugated to streptavidin was added, and after washing six times, the time-resolved fluorescence signal was measured via a BMG PHERAstar plate reader (BMG LATECH). The detailed procedure and methods were reported in the previous studies.^[40,42]

2.9. Statistical Analysis

Statistical analyses between experimental groups were performed using Prism-4 software V4.03 (Graph Pad, San Diego, CA). In experiments with more than two experimental groups one-way ANOVA with Tukey’s post-test was used. P-values less than 0.05 are considered significant (* $p < 0.05$, ** $p < 0.01$, *** $p < 0.001$). Bar graphs depict mean \pm SD of n measures as detailed in figure legends.

3. Results and Discussion

Configuration and mechanism of the Acoustofluidic Centrifuge for EV (ACEV)

Figure 1a shows the configuration of the ACEV device. A 128° Y-cut lithium niobate (LiNbO_3) substrate is bonded with a ring made by polydimethylsiloxane (PDMS), which accommodates EV samples. An interdigital electrode patterned on a thin-film printed circuit board (TPCB) is mounted onto the LiNbO_3 substrate to produce SAWs travelling toward the EV sample loaded to the PDMS ring. By setting the angle between the electrode and the reference flat of the LiNbO_3 substrate to be 120° , a combination wave integrating Rayleigh and SH-SAWs is produced, which induces single vortex streaming and complex acoustic attenuation, effectively concentrating nanoparticles and EVs from the sample. The ACEV device offers a simple and accessible option to concentrate nanoparticles and EVs with ultrafast and low-volume fashions. The straightforward operation involves five steps, as shown in Figure 1b. (1) Cleaning and sterilizing the PDMS ring inside-out. (2) Loading an EV culture supernatant of approximately 50 μL to the PDMS ring. (3) Starting the concentration process by switching on the SAW. (4) An EV pellet is formed at the centre of the sample within 35 s. (5) Extracting the EV pellet by using a pipette. The concentrated EVs are ready for downstream analysis.

The ACEV device takes the advantage of the detachable electrodes when developing SAW devices,^[34] e.g., easy fabrication without accessing cleanroom facilities. The detachability feature allows rotation of the LiNbO_3 substrate to achieve arbitrary angles between the finger electrode and the reference flat of the substrate (Figure 2a). Such flexibility is essential in this study as it enables the investigation of potential SAW modes apart from Rayleigh and SH-SAWs. Due to the contact impedance existing between the electrodes and the

LiNbO₃ wafer, the TPCB-IDT yields less power efficiency than that made by the conventional photolithography process. This can be overcome by adding a matching network to the TPCB-IDT to improve impedance mismatching.^[34,35] Conventional SAW devices made using the photolithography process are often a one-off component, e.g., any modification to the IDT requires restarting the photolithography process, which limits the research throughput and increases the footprint of the device.

As the 128° Y-cut LiNbO₃ substrate is highly anisotropic, the generation of Rayleigh SAW requires the interdigital electrodes to be positioned in parallel with the reference flat of the LiNbO₃ substrate, which is annotated as $\gamma_1 = 0^\circ$ in Figure 2a. The diffraction of the acoustic wave causes the bulk fluid to translate along the direction of the SAW and exhibit Stokes Drag force on the suspended particles. The existence of the PDMS ring limits the translation leading to circular streaming produced inside the boundary when positioning the TPCB-IDT asymmetrically with an offset to the droplet center (Figure 1a & 2a).^[27,43] The particles in the droplet experience slower circular streaming velocity in the center resulting in a stagnation point established to accumulate the particle pellet.

3.1. The Generation of Various Wave Modes in the ACEV Device

Exploration of the ACEV device for generating potential wave modes was done by numerical studies in COMSOL. Three IDT angles, i.e., $\gamma_1 = 0^\circ$, $\gamma_2 = 90^\circ$, and $\gamma_3 = 120^\circ$, were simulated as the results shown in Figure 2b. For the angle $\gamma_1 = 0^\circ$, a typical out-of-plane surface displacement for generating Rayleigh SAW is achieved, in which the wave decays with a characteristic length approximately equal to a wavelength below the surface. The wave mode for the $\gamma_2 = 90^\circ$ reveals displacements in the plane of the surface and a compressional component, which highlights the presence of Quasi SH-SAWs.^[44] The SH-SAW has the advantage of virtually no acoustic loss in water, offering the potential to handle the EV sample. The vibration pattern where the $\gamma_3 = 120^\circ$ demonstrates the out-of-plane surface displacement and internal compressional components. This scenario establishes a dual-wave mode combining the advantage of the Rayleigh and SH-SAWs. Other angles during the rotation are beyond the discussion as they did not produce a notably valuable concentration effect.

The numerical studies of the SAW interaction with the droplet under the above three scenarios, i.e., $\gamma_1 = 0^\circ$, $\gamma_2 = 90^\circ$, and $\gamma_3 = 120^\circ$, are given in Figure 2c, where the 3-D models visualize the vibration amplitude on the LiNbO₃ substrate and the acoustic pressure within the sessile droplet. For $\gamma_1 = 0^\circ$ (Figure 2c, left), upon contact with the droplet, the Rayleigh SAW produces a leaky SAW with a Rayleigh angle of $\sim 22^\circ$ due to the acoustic energy attenuation into the fluid (Figure S2, Supporting Information). A notable emergence of the SH-SAW component on the x-y plane appears when $\gamma_2 = 90^\circ$ (Figure 2c, middle), resulting in symmetrical and radial acoustic pressure distribution within the droplet. In contrast to Rayleigh SAW attenuation, the SH-SAW induces sound waves in the droplet directly upwards (Figure S3, Supporting Information). For $\gamma_3 = 120^\circ$ (Figure 2c, right), the SH-SAW component is slightly

weaker than that in $\gamma_2 = 90^\circ$, which may imply a balance of generating both the Rayleigh and SH-SAW. A more intensive acoustic pressure distributed in the droplet is observed due to both the Rayleigh leaky SAW and the SH-SAW longitudinal components propagated in the droplet. The side view simulation of angle γ_3 (Figure S4, Supporting Information) also reveals that the droplet possesses both (Rayleigh and SH-SAW) components of acoustic attenuation. The combination of both modes, namely dual-wave acoustofluidic field, is a complex wave attenuated in the droplet resulting in an ultrafast concentration of nanoparticles.

3.2. Identification of the Working Frequency

To identify the working frequency of the RF signal of the three scenarios to drive the ACEV device the reflection coefficients (S_{11}) for each setup were measured. Figure 2d, left shows a dominating Rayleigh SAW frequency (green arrow) around 20 MHz with a minor SH-SAW component (blue arrow) close to 35 MHz. At $\gamma_2 = 90^\circ$, a dominant SH-SAW is observed (~ 34.4 MHz) with a minor component of a Rayleigh SAW. The SH-SAW frequency appears higher than the Rayleigh component as observed in substrate studies.^[45] A transition state between the Rayleigh and SH-SAW at $\gamma_3 = 120^\circ$ is identified with the working frequency of 32.8 MHz to potentially produce both waves (Figure 2d, right).

3.3. Acoustic Wave Induced Droplet Deformation and Nanoparticle Concentration

The deformation of the droplet surface induced by the interaction with the acoustic waves at the center (red curve) and the periphery (green and blue curves) is shown in Figure 2e. The Rayleigh SAW ($\gamma_1 = 0^\circ$) slightly increases the height of the droplet at the three locations showing no nanoparticle concentration effect as no aggregation observed under the fluorescence microscope (Figure 2e, left, also Video S1, Supporting Information). The SH-SAW ($\gamma_2 = 90^\circ$) leads to a considerable rise at the droplet center (up to 60%) and an intensive droplet jetting effect. Particle accumulation is vividly observed (white arrow, inset in Figure 2e, middle, also Video S1, Supporting Information). It is worth noting that this mode often led to intensive evaporation, making it unsuitable for manipulating biological samples. The findings agree with previous results,^[44] where the Rayleigh SAW was compared directly with SH-SAW.

The dual-wave mode taking place at $\gamma_3 = 120^\circ$ shows considerable improvement. As shown in Figure 2e, right (also Video S1, Supporting Information), the droplet surface denotes a notably increased height at the center with an oscillation pattern on the periphery. The nanoparticles are successfully concentrated in the center of the droplet (yellow arrow). It is predicted that a slight rise of the droplet height at the center, while oscillation on the sides, is the key to the effective concentration of nanoparticles. Conspicuously, droplet fluctuation under this dual-wave mode causes unnoticeable evaporation, which is essential for maintaining sample integrity and end-product extraction.

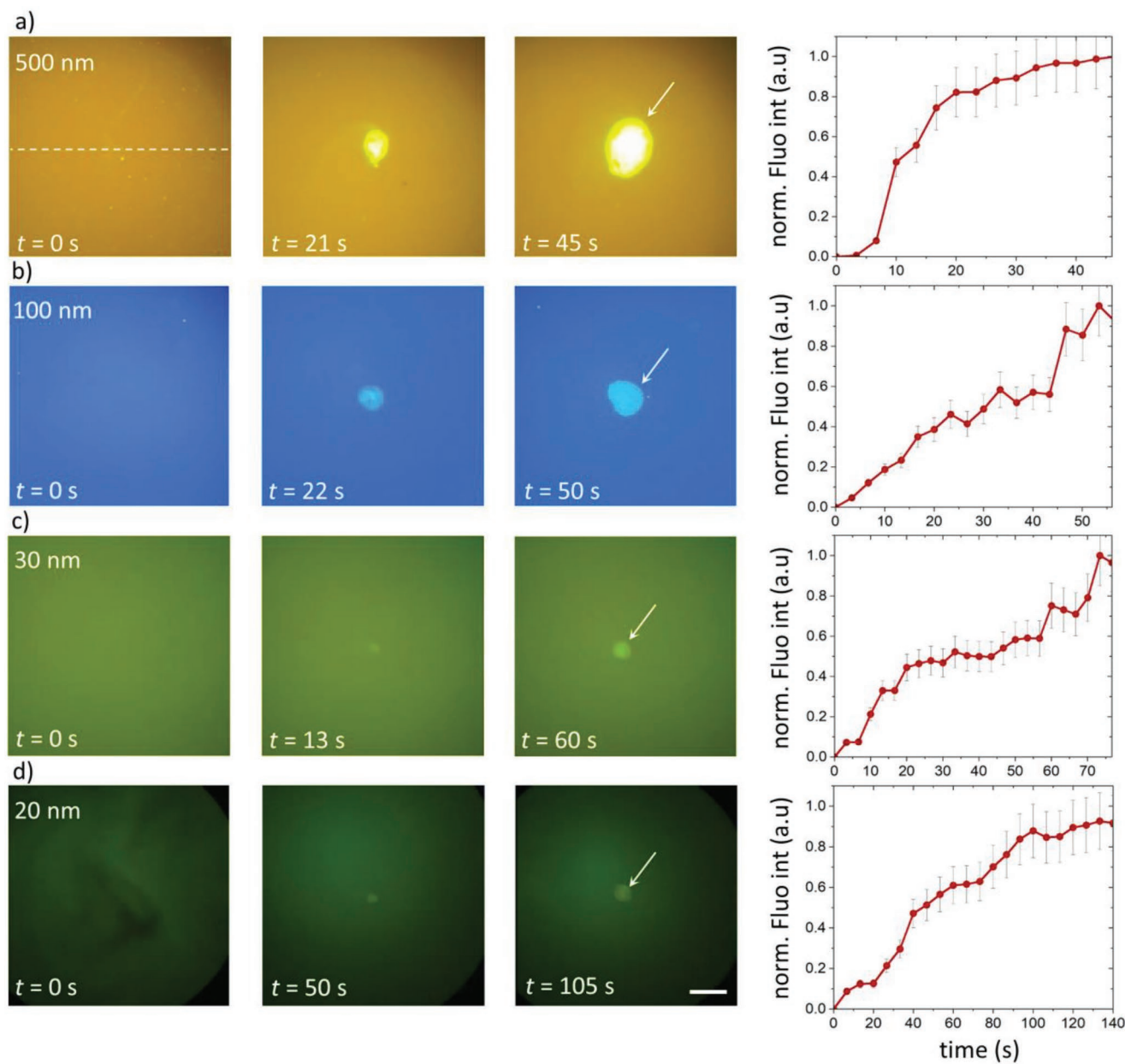


Figure 3. The concentration of nanoparticles with the size of 500 nm, 100 nm, 30 nm, and 20 nm, using the ACEV device. Fluorescence images of the sample with timestamps and the corresponding normalized fluorescence intensity ($n = 5$) are shown for a) 500 nm, b) 100 nm, c) 30 nm, and d) 20 nm nanoparticles. The dashed line highlights the measurement area. The scale bar is 0.5 mm.

3.4. Ultrafast Concentration of Nanoparticles

Nanoparticles with sizes of 20, 30, 100, and 500 nm were used to test the concentration capability of the ACEV device, as these sizes cover a wide range of EV sub-populations.^[46] As shown in **Figure 3**, fluorescence images with time scales provide a visual indication of the aggregation of the nanoparticles (white arrows in **Figure 3**, also in Videos S2–S5). For all the particle sizes, concentration was observed as soon as the SAW was applied. The normalized fluorescence intensity (norm. Fluo int) across the sample (dashed line in **Figure 3a**, left) was obtained to reveal the change in fluorescence intensity over time, as shown in

Figure 3. Durations for concentrating the four particle sizes are 45 s, 50 s, 60 s, and 105 s, respectively. Nanoparticles were found to be aggregated at the bottom in the center of the droplet (**Figure 2b**). These associated speeds represent a significant advance in the field of nanoparticle manipulation, enabling the concentration of a wide range of particle sizes with remarkable speed and precision. Achieving such precision and reproducibility in nanoparticle concentration is notoriously challenging with existing methods. Advances, brought by ACEV have important implications for nanoparticle research, enabling more accurate and efficient analysis of sub-populations and potentially leading to new insights into their properties and applications.

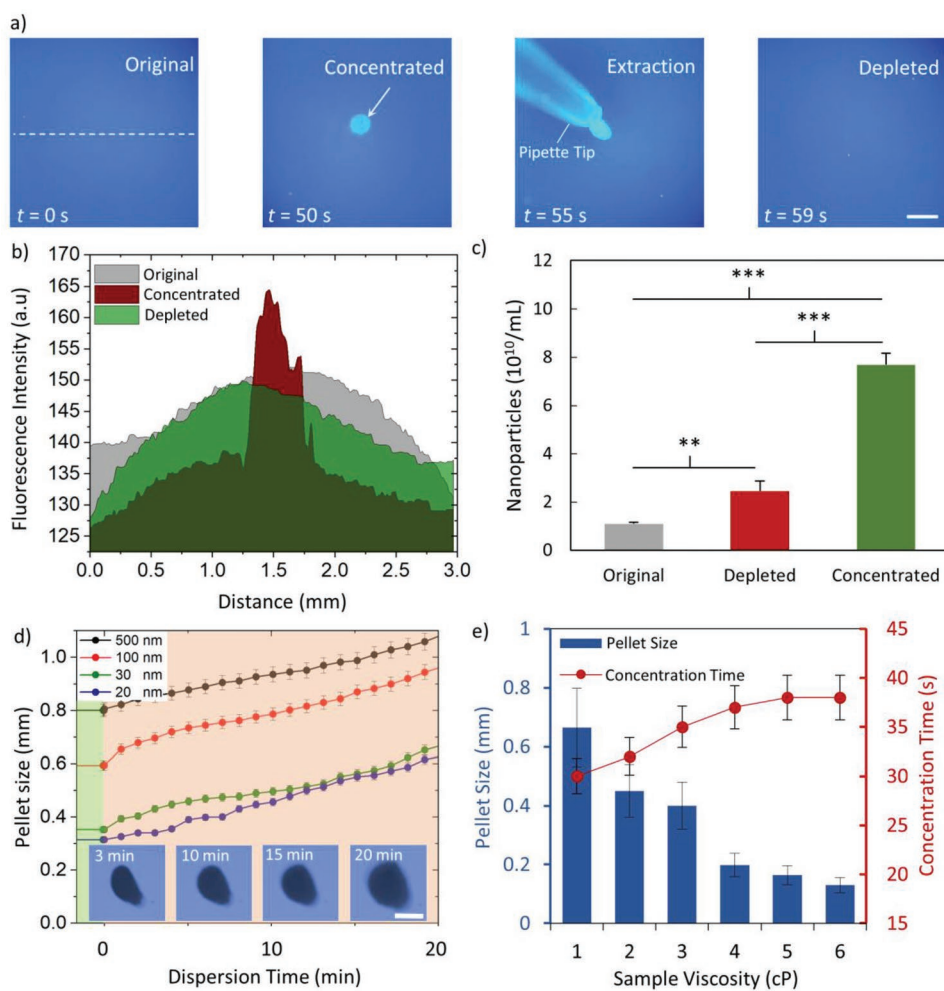


Figure 4. The concentration and extraction of nanoparticles in the ACEV device. a) Fluorescence images of the original sample, concentration, during extraction, and depleted samples. The nanoparticle size is 100 nm. Scale bar 0.5 mm. b) Fluorescence intensity of the sample upon the sequential steps. c) Nanoparticle tracking analysis was performed to establish the nanoparticle density of the original sample, concentrated collection, and depleted sample. ($n = 3$, $***p < 0.001$, 1-way Anova with Tukey's post-test). d) The pellet size changes over time; the inset is the dispersion of the 500-nm particle pellet over 20 min. Scale bar 1 mm. e) The concentration time for nanoparticles over various sample viscosities.

3.5. Pellet Extraction and Concentration Performance

It is essential to have a simple extraction modality to collect the enriched EVs from the ACEV device for downstream applications, ideally using conveniently accessible tools such as pipettes. As shown in **Figure 4a** (also in Video S6, Supporting Information), the nanoparticles are well concentrated in a pellet after ≈ 50 s of SAW exposure. A pipette tip is placed near the pellet with guidance under the microscope. The plunger is then slowly released to extract a sample of 0.5 μ L, resulting in the nanoparticle pellet being pulled up into the tip.

To assess the concentration and extraction ability of the ACEV device, the fluorescence intensity of the original, concentrated, and depleted samples, was measured as shown in **Figure 4b**. Before concentration, the fluorescence signal indicates the presence of randomly dispersed nanoparticles (grey area). After SAW concentration, a sharp spike in fluorescence intensity is observed at the centre of the droplet (red area), corresponding to the highly concentrated nanoparticles in the

pellet. After pipette extraction, the intensity levels off, indicating a complete collection of the pellet. Nanoparticle tracking analysis (NTA) was used to further confirm the extraction completion. As shown in **Figure 4c**, the nanoparticle density in the pellet increases to 7.69×10^{10} , from the original sample of 1.11×10^{10} , which describes the concentration capability of the ACEV device.

The nanoparticle pellet's integrity over time after the concentration is important to design the follow-up collection processes. **Figure 4d** shows the pellet size of the four sizes of nanoparticles over 20 min after the ACEV concentration. In general, the pellet presents an average enlargement of $\sim 50\%$ after 20 min but only $\sim 7\%$ over 3 min. This should be sufficient to streamline most manual or automatic extraction processes. The whole processing time from the beginning of the ACEV concentration to pellet extraction takes less than one minute. This is a step change in nanoparticle concentration, in contrast to ultracentrifugation, or an assortment of other modalities that are well-known as a time-consuming and labor-intensive process.

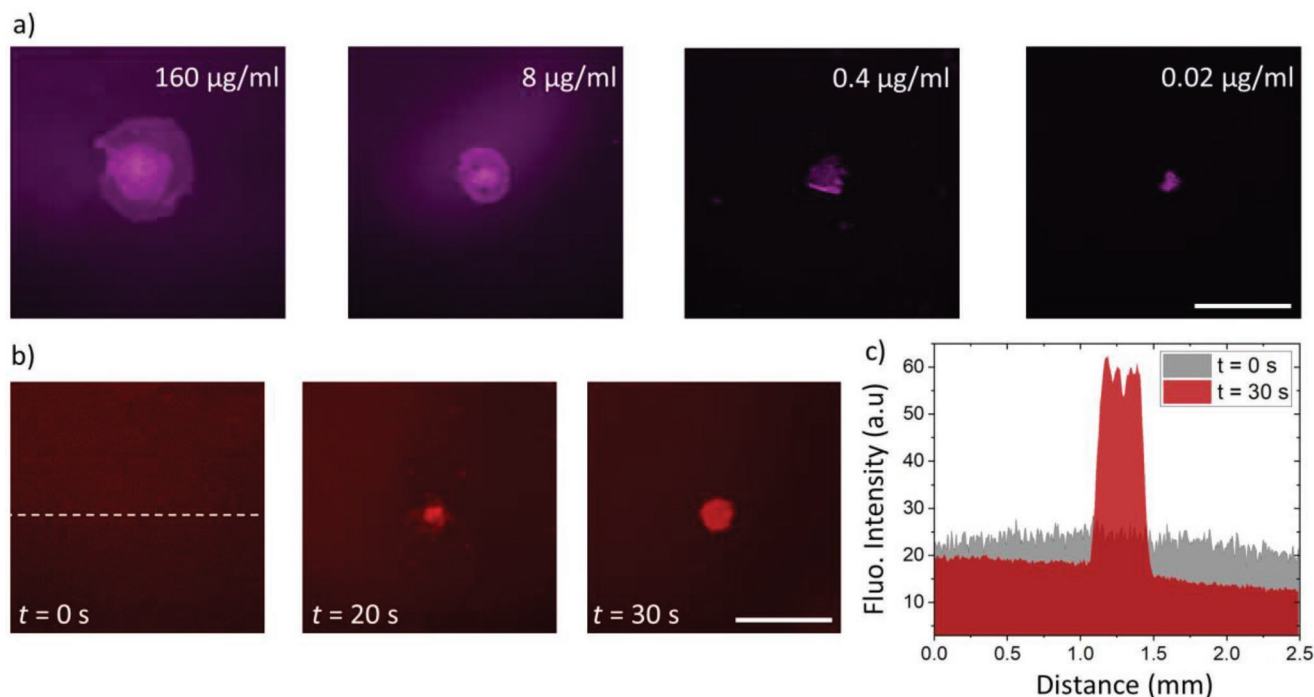


Figure 5. EV concentration using the ACEV device. a) Four EV dilutions are concentrated by using the ACEV device. b) The EV sample of $0.4 \mu\text{g mL}^{-1}$ is enriched within 30 s. c) The normalized fluorescence intensity in the EV sample ($0.4 \mu\text{g mL}^{-1}$) before and after SAW concentration. Scale bars 1 mm.

To explore the concentration time for samples with various viscosities, the nanoparticle suspension was conditioned by adding glycerol to achieve a viscosity of 1 to 6 cP, which encompassed the range of several body fluids, including cerebrospinal fluid (~ 1 cP) and whole blood (4–5 cP).^[47] The SAW concentration was processed on these samples with the result shown in Figure 4e. The time required to concentrate the nanoparticles increased slightly from 30 s to 37 s when the sample became more viscous, which also impacted the efficacy of the concentration. For instance, at viscosities higher than 4 cP, similar to whole blood, it is struggled to observe nanoparticle pellets perceptibly. The sample used in most of the experiments in the study mimicked the viscosity of cell culture supernatant, i.e., 1.1 cP, which fell in the recommended viscosity range (0.5 – 3 cP) of the ACEV concentration.

3.6. EV Enrichment in ≈ 30 Seconds

After systematic characterization of the ACEV device, EV samples with four dilutions ($160, 8, 0.4, 0.02 \mu\text{g mL}^{-1}$) were applied to test the ACEV handling biological samples. It is notoriously difficult to estimate whether or not this concentration range is physiologically relevant, because as yet the EV field lacks definitive tools to specifically quantify vesicles, as opposed to other forms of particulates, present in body fluids.^[48] This range would certainly serve a variety of scenarios from cell culture soups and is likely appropriate for different forms of biofluids.

The wide-field fluorescence images shown in Figure 5a present the concentration of EVs labelled with a fluorophore. The concentration process was somewhat similar to the nanoparticles, as an immediate EV aggregation occurred soon after

applying the dual wave. Whatever dilutions, the ACEV device could concentrate the EVs within approximately 30 s with the sample volume of $50 \mu\text{L}$, which is a tenfold increase in the volume handled by the state-of-the-art technique reported in.^[31]

The formation of the EV pellet ($0.4 \mu\text{g mL}^{-1}$ sample) was recorded as shown in Figure 5b, EV aggregation becomes evident and visible in the droplet center after only 20 s. The fluorescence intensity reaches the plateau at ≈ 30 s (Figure 5c), denoting the completion of the pellet. The pipette was used to extract a $0.5 \mu\text{L}$ sample to collect the EV pellet for follow-up analysis. The total time from sample loading to EV pellet harvest was again less than 1 min. Observationally, the shape of the concentrated EVs was not uniformly round as for polystyrene nanoparticles, and certainly at higher concentrations present a shape that has a central bright core, surrounded by a more diffuse outer ring, akin to a “fried egg” (Figure 5a). We are uncertain why this is occurring but is likely due to the heterogeneity of EVs present in the sample, reflecting differences in size, densities, and molecular composition.

3.7. EV Characterization after ACEV Concentration

Maintaining EV integrity and function is critical when developing any EV manipulation technique or device. Apart from the EV concentration efficiency provided in Figure 5, the following measurements were performed to systematically study the effects of the ACEV device on the EVs. Firstly, cryo-electron microscopy (cryo-EM) was used to check the existence of EVs and their structural features. The cryo-EM images of nanoparticles extracted from the control specimen (not subject to ACEV), post ACEV concentrated zone (pellet), and post ACEV depleted

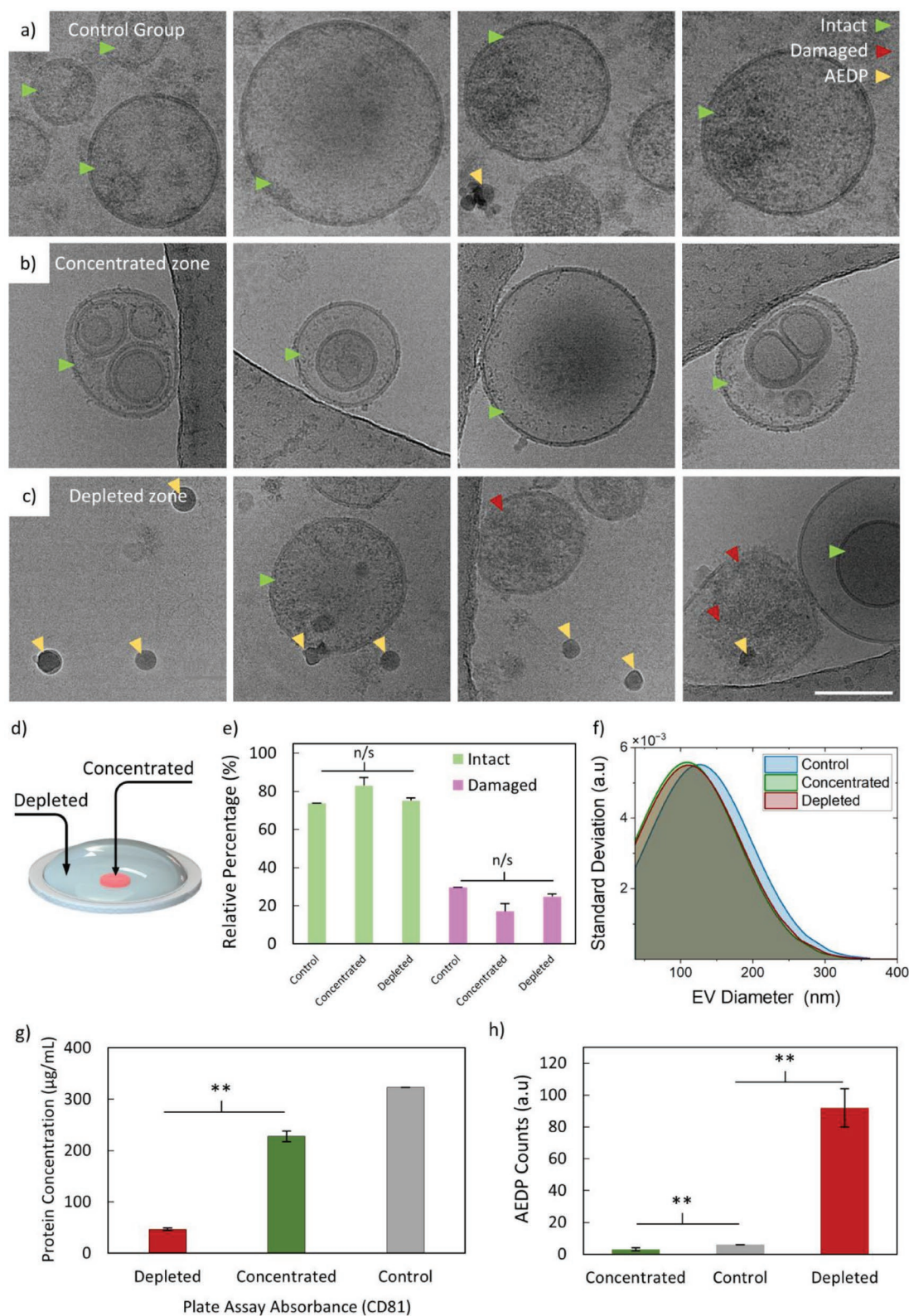


Figure 6. Analysis of the EV samples concentrated by using the ACEV device. a) Gallery for cryo-electron microscopy (cryo-EM) imaging showing the nanoparticles in the a) control group, b) concentrated region, and c) depleted region, scale bar 100 nm. d) Indication of different sampling regions of the device. e) Relative proportions of intact and damaged vesicles from a pool of cryo-EM images (>40 microscopic fields per condition), where there were no significant differences found. f) Measurement of size variation taken from the cryo-EM images (n = 611). g) Relative concentration of CD81-positive EV (n = 2). h) Numerical count of avascular electron-dense particles (AEDP) in samples (n = 2). Significance determined by 1-way Anova, with Tukey's post test, where *p<0.05, **p<0.01, ***p<0.001.

zone are shown in **Figure 6a**. The definition of the concentrated zone and the depleted zone is illustrated in **Figure 6b**. According to our observations, the nanoparticles in these collections are classified into: intact (green arrows), damaged (red arrows), and avescicular electron-dense particle (AEDP) (yellow arrows). We define “intact” as a rounded structure, in which the outer lipidic membrane is fully contiguous, with no evidence of gaps, disturbance or any perturbation hence the outside of the vesicle is truly separated from the inner luminal compartment by this integral membrane structure. For vesicles that appear to encapsulate other membrane-structures (vesicles within vesicles), our definition of “intact” focuses only on the outer membrane and does not consider possible perturbations of the encapsulated structures. For the term “damaged”, we observe examples where this outer lipidic membrane has indeed been compromised and is not contiguous. Often this reveals a possibility of a spill-out of content from the vesicle as further evidence of loss of integrity of the structure. Our definition of avescicular particles is based on the presence of dark nanoscale structures that lack evidence of a lipidic membrane, and although considered to be formed of protein and possibly other aggregated biomolecules their precise nature is not well known. Similar avescicular structures have, however, been reported elsewhere.^[49]

Representative images from the control group depict a variety of nanoscale yet heterogeneous vesicular structures with clearly delineated membrane boundaries that are circular and contiguous (green arrows), as intact vesicles. Some amorphous materials and rare AEDPs (yellow arrows) that lack membranes are occasionally observed. **Figure 6b,c** show the representative images from the samples subjected to acoustic pressures from the concentrated and depleted zones. A heterogeneous EV population within the concentrated zone with contiguous membranes can be observed (green arrows). Although the amorphous background material is still present, it is much less commonly observed than in the control group. The AEDPs, however, are not observed in this sample, and this was an unexpected yet highly desirable finding, as the ACEV appears therefore to remove these other types of particles from the EV concentrate. For the depleted zone, morphologically intact and damaged membranes (red arrows) were present together with a relative abundance of AEDP.

Quantification of these images across over 40 regions of interest per specimen revealed that, on average, 75% of vesicles are classified as intact (**Figure 6e**). The proportions of damaged membranes in the Control and acoustic exposure groups are broadly comparable and hence this damage is most likely due to the processes in specimen handling before the ACEV concentration. These results reveal that the ACEV device has a minor impact on EV membrane integrity and does not, therefore, cause significant perturbation to the EV structure. The EV measurements ($n = 611$) revealed a comparable size distribution, indicating no vesicle size-based selectivity in the concentration process (**Figure 6f**).

For many reasons, estimating a concentration effect by cryo-EM would be unreliable, and hence we used an orthogonal method to confirm that the ACEV device has indeed concentrated EVs, and not merely the fluorophore-related material. For this, we measured the vesicle-associated protein in the specified

regions of the device. CD81 is a well-established EV biomarker highly abundant on the EV surface and is not a protein shed into the secretome of cells. Therefore, detecting the presence of CD81 would be a surrogate measure of the presence of vesicles. This was measured using an ELISA-like assay, with a standard curve generated using purified Du145 EVs. **Figure 6g** shows that from an initial vesicle concentration of $129 \mu\text{g mL}^{-1}$ of CD81-positive vesicles, EVs are successfully concentrated by the ACEV device to $237 \mu\text{g mL}^{-1}$ in the concentration zone. In contrast, the depleted zone had a reduction of CD81-positive vesicles to $<50 \mu\text{g mL}^{-1}$, reflecting an 85% difference in CD81 (and hence EVs) between the concentrated and depleted zones.

Lastly, looking closely at the cryo-EM images, we noticed significant differences (** $p < 0.01$) of 15–20 nm sized AEDPs present in the depleted region (see the yellow arrow in **Figure 6c** as an example). Such particle size is at the exact threshold of the ACEV current limitations (≈ 20 nm). In fact, the vast majority of these structures were present, and arguably concentrated within the depleted zone (**Figure 6h**). It is not the first time that AEDPs have been identified from cryo-EM imaging, as these structures have been reported in many other studies.^[50–52] Assuming AEDPs are undesirable from an EV-purification perspective, the ACEV device supplies the additional advantage of separating potentially detrimental aggregates while simultaneously concentrating intact EVs in less than a minute.

4. Conclusion

The ACEV device for ultrafast concentration of EVs based on acoustofluidics was developed using the accessible TPCB technique. The dual-wave mode simultaneously producing Rayleigh and SH-SAWs on the ACEV device enabled effective concentration of nanoparticles down to the size of 20 nm. The sample volume of 50 μL was processed with a range of nanoparticle sizes, followed by EV (derived from human prostate cancer (Du145) cell line) aggregation in a pellet in less than 35 seconds. More importantly, the ACEV device demonstrated a significant advantage in maintaining EV integrity during concentration and enormous convenience for extracting enriched particles with the added potential of excluding undesirable protein aggregates. The concentration effect of this proof-of-concept EV device was influenced not only by the device's performance but also, to a considerable extent, by the manual dexterity needed at the collection from the concentrated zone. Therefore, more refined, and automated iterations will be needed to enhance the system's concentration performance and throughput.

Supporting Information

Supporting Information is available from the Wiley Online Library or from the author.

Acknowledgements

The authors thank CIC bioGUNE Electron Microscopy Platform for their technological assistance.

Conflict of Interest

The authors declare no conflict of interest.

Data Availability Statement

The data that support the findings of this study are available on request from the corresponding author. The data are not publicly available due to privacy or ethical restrictions.

Keywords

extracellular vesicles, nanoparticles, printed circuit boards, surface acoustic waves

Received: January 13, 2023

Revised: March 30, 2023

Published online:

- [1] R. Isaac, F. C. G. Reis, W. Ying, J. M. Olefsky, *Cell Metab.* **2021**, *33*, 1744.
- [2] R. Kalluri, V. S. Lebleu, *Science* **2020**, *367*, eaau6977.
- [3] P. D. Stahl, G. Raposo, *Physiology* **2019**, *34*, 169.
- [4] L. Mashouri, H. Yousefi, A. R. Aref, A. M. Ahadi, F. Molaei, S. K. Alahari, *Mol Cancer* **2019**, *18*, 75.
- [5] L. Bouchareychas, P. Duong, S. Covarrubias, E. Alsop, T. A. Phu, A. Chung, M. Gomes, D. Wong, B. Meechoovet, A. Capili, R. Yamamoto, H. Nakauchi, M. T. Mcmanus, S. Carpenter, K. Van Keuren-Jensen, R. L. Raffai, *Cell Rep.* **2020**, *32*, 107881.
- [6] Le Zhu, H.-T. Sun, S. Wang, S.-L. Huang, Y. Zheng, C.-Q. Wang, B.-Y. Hu, W. Qin, T.-T. Zou, Y. Fu, X.-T. Shen, W.-W. Zhu, Y. Geng, Lu Lu, Hu-L. Jia, L.-X. Qin, Q.-Z. Dong, *J. Hematol. Oncol. J Hematol Oncol* **2020**, *13*, 152.
- [7] J. Zhu, B. Liu, Z. Wang, Di Wang, H. Ni, L. Zhang, Yi Wang, *Theranostics* **2019**, *9*, 6901.
- [8] S. Zhao, Y. Mi, B. Guan, B. Zheng, P. Wei, Y. Gu, Z. Zhang, S. Cai, Ye Xu, X. Li, X. He, X. Zhong, G. Li, Z. Chen, D. Li, *J. Hematol. Oncol. J Hematol Oncol* **2020**, *13*, 156.
- [9] L. Zhu, S. Kalimuthu, P. Gangadaran, Ji M Oh, Ho W Lee, Se H Baek, S. Y. Jeong, S.-W. Lee, J. Lee, B.-C. Ahn, *Theranostics* **2017**, *7*, 2732.
- [10] A. Bobrie, M. Colombo, S. Krumeich, G. Raposo, C. Théry, *J. Extracell Vesicles* **2012**, *1*, 18397.
- [11] R. J. Lobb, M. Becker, S. Wen Wen, C. S. F. Wong, A. P. Wiegman, A. Leimgruber, A. Möller, *J. Extracell Vesicles* **2015**, *4*, 27031.
- [12] A. N. Böing, E. Van Der Pol, A. E. Grootemaat, F. A. W. Coumans, A. Sturk, R. Nieuwland, *J. Extracell Vesicles* **2014**, *3*, 23430.
- [13] S. Sitar, A. Kejžar, D. Pahovnik, K. Kogej, M. Tušek-Žnidarič, M. Lenassi, E. Žagar, *Anal. Chem.* **2015**, *87*, 9225.
- [14] A. H. J. Yang, S. D. Moore, B. S. Schmidt, M. Klug, M. Lipson, D. Erickson, *Nature* **2009**, *457*, 71.
- [15] S.-I. Han, H. Soo Kim, A. Han, *Biosens. Bioelectron.* **2017**, *97*, 41.
- [16] J. Zeng, C. Chen, P. Vedantam, T.-R. Tzeng, X. Xuan, *Microfluid Nanofluidics* **2013**, *15*, 49.
- [17] L. Wang, D. S. Dandy, *Adv. Sci.* **2017**, *4*, 1700153.
- [18] S.-C. S. Lin, X. Mao, T. J. Huang, *Lab Chip* **2012**, *12*, 2766.
- [19] Y. Xie, J. Rufo, R. Zhong, J. Rich, P. Li, K. W. Leong, T. J. Huang, *ACS Nano* **2020**, *14*, 16220.
- [20] J. Rufo, F. Cai, J. Friend, M. Wiklund, T. J. Huang, *Nat. Rev. Methods Primers* **2022**, *2*, 30.
- [21] Y. Gu, C. Chen, J. Rufo, C. Shen, Z. Wang, Po-H Huang, H. Fu, P. Zhang, S. A. Cummer, Z. Tian, T. J. Huang, *ACS Nano* **2020**, *14*, 14635.
- [22] Y. Q. Fu, J. K. Luo, N. T. Nguyen, A. J. Walton, A. J. Flewitt, X. T. Zu, Y. Li, G. Mchale, A. Matthews, E. Iborra, H. Du, W. I. Milne, *Prog. Mater. Sci.* **2017**, *89*, 31.
- [23] Y.-Q. Fu, H.-F. Pang, H. Torun, R. Tao, G. Mchale, J. Reboud, K. Tao, J. Zhou, J. Luo, D. Gibson, J. Luo, P. Hu, *Lab Chip* **2021**, *21*, 254.
- [24] F. Martin, M. I. Newton, G. Mchale, K. A. Melzak, E. Gizeli, *Biosens. Bioelectron.* **2004**, *19*, 627.
- [25] H. Li, J. R. Friend, L. Y. Yeo, *Biomed. Microdevices* **2007**, *9*, 647.
- [26] P. R. Rogers, J. R. Friend, L. Y. Yeo, *Lab Chip* **2010**, *10*, 2979.
- [27] G. Destgeer, H. Cho, B. H. Ha, J. Ho Jung, J. Park, H. J. Sung, *Lab Chip* **2016**, *16*, 660.
- [28] N. Zhang, J. P. Zuniga-Hertz, E. Y. Zhang, T. Gopesh, M. J. Fannon, J. Wang, Y. Wen, H. H. Patel, J. Friend, *Lab Chip* **2021**, *21*, 904.
- [29] Z. Mao, P. Li, M. Wu, H. Bachman, N. Mesyngier, X. Guo, S. Liu, F. Costanzo, T. J. Huang, *ACS Nano* **2017**, *11*, 603.
- [30] P. Liu, Z. Tian, N. Hao, H. Bachman, P. Zhang, J. Hu, T. J. Huang, *Lab Chip* **2020**, *20*, 3399.
- [31] Y. Gu, C. Chen, Z. Mao, H. Bachman, R. Becker, J. Rufo, Z. Wang, P. Zhang, J. Mai, S. Yang, J. Zhang, S. Zhao, Y. Ouyang, D. T. W. Wong, Y. Sadovskiy, T. J. Huang, *Sci. Adv.* **2021**, *7*, eabc0467.
- [32] Z. Wang, J. Rich, N. Hao, Y. Gu, C. Chen, S. Yang, P. Zhang, T. J. Huang, *Microsyst. Nanoeng.* **2022**, *8*, 45.
- [33] C. Sun, R. Mikhaylov, Y. Fu, F. Wu, H. Wang, X. Yuan, Z. Xie, D. Liang, Z. Wu, X. Yang, *IEEE Trans. Electron Devices* **2021**, *68*, 393.
- [34] R. Mikhaylov, F. Wu, H. Wang, A. Clayton, C. Sun, Z. Xie, D. Liang, Y. Dong, F. Yuan, D. Moschou, Z. Wu, M. H. Shen, J. Yang, Y. Fu, Z. Yang, C. Burton, R. J. Errington, M. Wiltshire, X. Yang, *Lab Chip* **2020**, *20*, 1807.
- [35] R. Mikhaylov, M. S. Martin, P. Dumcius, H. Wang, F. Wu, X. Zhang, V. Akhimi, C. Sun, A. Clayton, Y. Fu, L. Ye, Z. Dong, Z. Wu, X. Yang, *J. Micromechanics Microengineering* **2021**, *31*, 074003.
- [36] H. Ledbetter, H. Ogi, N. Nakamura, *Mech. Mater.* **2004**, *36*, 941.
- [37] M. S. Namnabat, M. Moghimi Zand, E. Houshfar, *Sci. Rep.* **2021**, *11*, 13326.
- [38] J. Webber, R. Steadman, M. D. Mason, Z. Tabi, A. Clayton, *Cancer Res.* **2010**, *70*, 9621.
- [39] C. Théry, S. Amigorena, G. Raposo, A. Clayton, *Curr Protoc Cell Biol* **2006**, *30*, <https://doi.org/10.1002/0471143030.cb0322s30>.
- [40] H. D. Roberts-Dalton, A. Cocks, J. M. Falcon-Perez, E. J. Sayers, J. P. Webber, P. Watson, A. Clayton, A. T. Jones, *Nanoscale* **2017**, *9*, 13693.
- [41] "J of Extracellular Vesicle –2021 – Shephard – Stroma-derived extracellular vesicle mRNA signatures inform histological.pdf."
- [42] J. Webber, T. C. Stone, E. Katilius, B. C. Smith, B. Gordon, M. D. Mason, Z. Tabi, I. A. Brewis, A. Clayton, *Mol. Cell. Proteomics* **2014**, *13*, 1050.
- [43] H. Nam, H. J. Sung, J. Park, J. S. Jeon, *Lab Chip* **2022**, *22*, 47.
- [44] C. Fu, A. J. Quan, J. T. Luo, H. F. Pang, Y. J. Guo, Q. Wu, W. P. Ng, X. T. Zu, Y. Q. Fu, *Appl. Phys. Lett.* **2017**, *110*, 173501.
- [45] H.-F. Pang, R. Tao, J. Luo, X. Zhou, J. Zhou, G. Mchale, J. Reboud, H. Torun, D. Gibson, K. Tao, H. Chang, Y.-Q. Fu, *Surf. Coat. Technol.* **2022**, *442*, 128336.
- [46] "J of Extracellular Vesicle –2015 – Y ez-M – Biological properties of extracellular vesicles and their physiological.pdf."
- [47] R. S. Rosenson, A. McCormick, E. F. Uretz, *Clin. Chem.* **1996**, *42*, 1189.
- [48] "Clayton et al., –2019 – Considerations toward a roadmap for collection, h.pdf."
- [49] H. Zhang, D. Freitas, H. S. Kim, K. Fabijanic, Z. Li, H. Chen, M. T. Mark, H. Molina, A. B. Martin, L. Bojmar, J. Fang,

- S. Rampersaud, A. Hoshino, I. Matei, C M. Kenific, M. Nakajima, A. P. Mutvei, P. Sansone, W. Buehring, H. Wang, J. P. Jimenez, L. Cohen-Gould, N. Paknejad, M. Brendel, K. Manova-Todorova, A. Magalhães, J. A. Ferreira, H. Osório, A M. Silva, A. Massey, et al., *Nat. Cell Biol.* **2018**, *20*, 332.
- [50] G. Raposo, W. Stoorvogel, *J. Cell Biol.* **2013**, *200*, 373.
- [51] P. D'acunzo, R. Pérez-González, Y. Kim, T. Hargash, C. Miller, M J. Alldred, H. Erdjument-Bromage, S C. Penikalapati, M. Pawlik, M. Saito, M. Saito, S D. Ginsberg, T A. Neubert, C N. Goulbourne, E. Levy, *Sci. Adv.* **2021**, *7*, eabe5085.
- [52] D. Zabeo, A. Cvjetkovic, C. Lässer, M. Schorb, J. Lötval, J. L. Höög, *J. Extracell Vesicles* **2017**, *6*, 1329476.